AGU PUBLICATIONS

Geophysical Research Letters

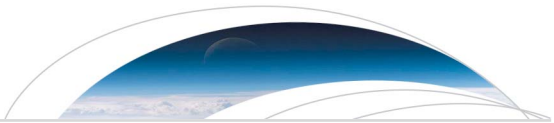

RESEARCH LETTER
10.1002/2016GL071061

Key Points:
- We use a Bayesian approach to identify fault geometry and slip rates compatible with geodesy and conservation of motion
- The surface velocity field in Southern California is in agreement with a large-scale decollement that partitions deep-seated motion
- Structural geology and long-term slip compatibility laws help constraining the kinematics of buried faults below Los Angeles

Supporting Information:
- Supporting Information S1

Correspondence to:
S. Barbot and S. Daout,
sbarbot@ntu.edu.sg;
simon.daout@univ-grenoble-alpes.fr

Citation:
Daout, S., S. Barbot, G. Peltzer, M.-P. Doin, Z. Liu, and R. Jolivet (2016), Constraining the kinematics of metropolitan Los Angeles faults with a slip-partitioning model, *Geophys. Res. Lett.*, *43*, 11,192–11,201 doi:10.1002/2016GL071061.

Received 9 JUN 2016
Accepted 23 OCT 2016
Accepted article online 28 OCT 2016
Published online 9 NOV 2016

Constraining the kinematics of metropolitan Los Angeles faults with a slip-partitioning model

S. Daout[1], S. Barbot[2], G. Peltzer[3,4], M.-P. Doin[1], Z. Liu[4], and R. Jolivet[5]

[1]ISTerre, Université Grenoble-Alpes, CNRS, Grenoble, France, [2]Earth Observatory of Singapore, Nanyang Technological University, Singapore, [3]Department of Earth Science, University of California, Los Angeles, California, USA, [4]Jet Propulsion Laboratory, California Institute of Technology, Pasadena, California, USA, [5]Laboratoire de Géologie, UMR 8538, Departement de Géosciences, École Normale Supérieure, PSL Research University, Paris, France

Abstract Due to the limited resolution at depth of geodetic and other geophysical data, the geometry and the loading rate of the ramp-décollement faults below the metropolitan Los Angeles are poorly understood. Here we complement these data by assuming conservation of motion across the Big Bend of the San Andreas Fault. Using a Bayesian approach, we constrain the geometry of the ramp-décollement system from the Mojave block to Los Angeles and propose a partitioning of the convergence with 25.5 ± 0.5 mm/yr and 3.1 ± 0.6 mm/yr of strike-slip motion along the San Andreas Fault and the Whittier Fault, with 2.7 ± 0.9 mm/yr and 2.5 ± 1.0 mm/yr of updip movement along the Sierra Madre and the Puente Hills thrusts. Incorporating conservation of motion in geodetic models of strain accumulation reduces the number of free parameters and constitutes a useful methodology to estimate the tectonic loading and seismic potential of buried fault networks.

1. Introduction

The Pacific Plate (PAP) made its first contact with the North America Plate (NAP) about 28 Ma ago, when the Farallon slab, which was separating them, fully subducted beneath the American continent. The San Andreas Fault (SAF) follows the previous suture zone of the downgoing Farallon slab beneath the western NAP [*Furlong and Hugo*, 1989] and accounts for a large fraction of the relative motion between the PAP and the NAP [*Lisowski et al.*, 1991; *Tong et al.*, 2013]. The crustal expression of this transform boundary in Southern California is complex and involves a large number of faults [*Plesch et al.*, 2007] with multiple strands [*Mount and Suppe*, 1992; *Teyssier and Tikoff*, 1998]. Most of the deformation along the SAF system is accommodated by long and mature strike-slip faults, but some of the relative convergence is absorbed by thrusts or oblique strike-slip faults [*Walls et al.*, 1998].

Despite the surface complexity of the SAF system, the far-field interseismic horizontal velocity field is relatively uniform along the SAF from the Coachella to the Mojave segment of the SAF (Figure 1a). GPS velocity vectors in the ITRF08 reference frame are closely aligned with the Coachella segment of the SAF and the San Jacinto Fault (SJF). Farther north, near the Mojave segment of the SAF, GPS velocity vectors between the Mojave Block and Los Angeles (LA) have a similar orientation, despite the remarkable change of strike of the SAF of 18° (blue vector PP′ of Figure 1b). The projection of this vector on the fault-perpendicular and fault-parallel directions indicates ~7 mm/yr of far-field contraction [*Bock et al.*, 1997; *Argus et al.*, 2005] (red vector of Figure 1b and Table S1 in the supporting information) and ~26 mm/yr of transform motion (black vector of Figure 1b and Table S1). This relatively uniform orientation of the surface velocity vectors in Southern California is in contradiction with the complex superficial geometry of the fault system and might be the result of slip partitioning in the middle and lower crust (Figure 1c) [*Mount and Suppe*, 1987; *Crouch and Suppe*, 1993; *Bowman et al.*, 2003]. At depth, the long-term average cumulative horizontal velocity vectors must be accommodated by the interplay of strike-slip and thrust faults.

Both the transform and convergent components of deformation are responsible for significant seismic hazard in Southern California [*Dolan et al.*, 1995; *Walls et al.*, 1998]. Strike-slip faults can generate long seismic ruptures, such as during the 1812 M_w 6.9 San Juan Capistrano and the 1857 M_w 7.9 Fort Tejon earthquakes [*Sieh*, 1978; *Toppozada et al.*, 2002], and reverse faulting is at the origin of the 1971 M_L 6.6 San Fernando, the 1987 M_L 5.9 Whittier Narrows, the 1991 M_L 5.8 Sierra Madre, and the 1994 M_w 6.7 Northridge earthquakes

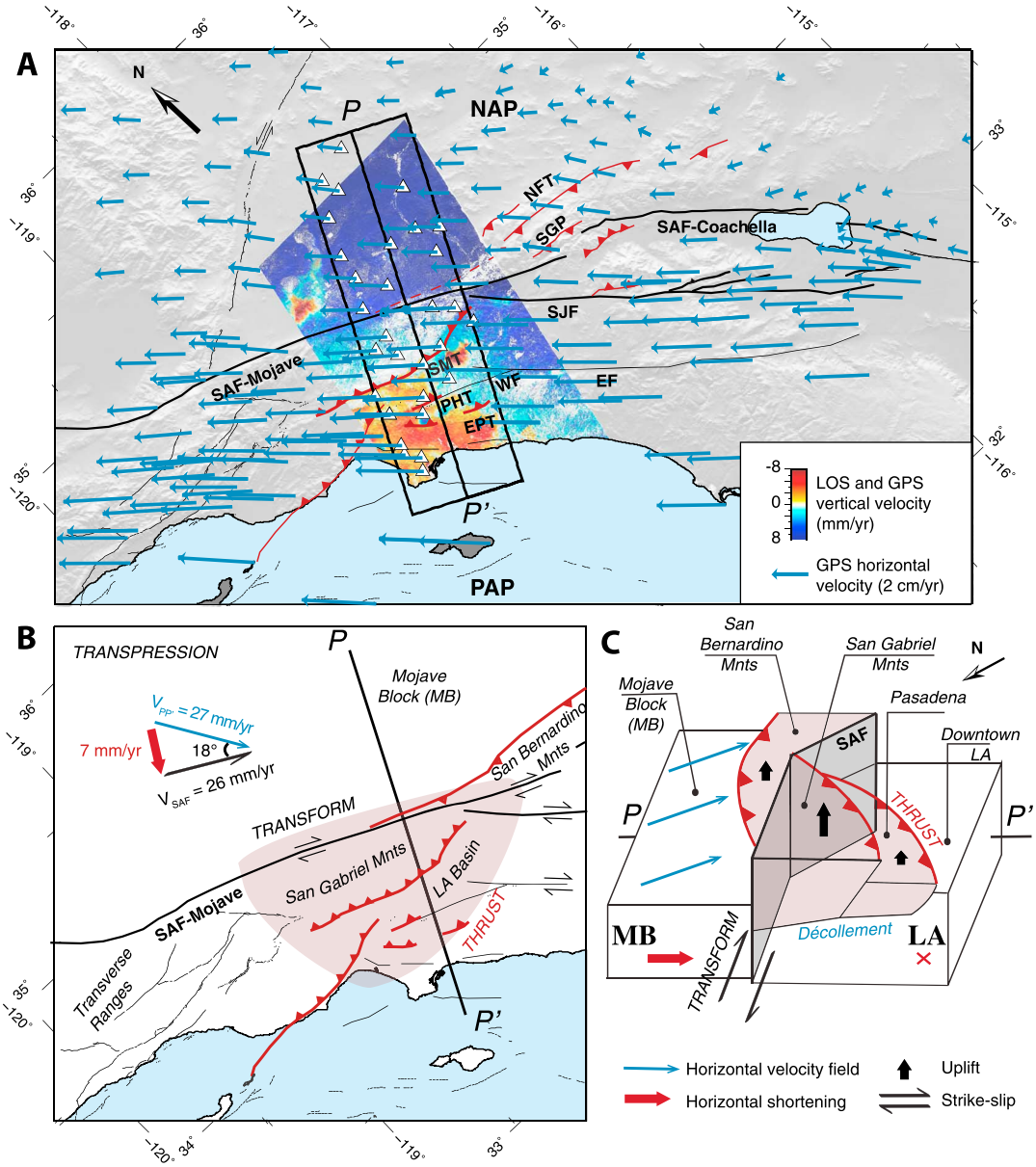

Figure 1. Seismotectonic setting of the Southern California fault system. (a) GPS data in the ITRF08 reference frame highlighting a uniform velocity field despite the complex three-dimensional geometry of the faults systems. InSAR velocitiy map is derived from Envisat descending track 170 [from *Liu et al.*, 2014]. Black rectangle defines the profile perpendicular to the SAF. Major strikes-slip faults including the San Andreas Fault (SAF), Whittier Fault (WF), San Jacinto Fault (SJF), and the Elsinore Fault (EF) are in black. Major thrust faults including the Sierra Madre Thrust fault (SMT), the Elysian Park Thrust (EPT), the Puente Hills Thrusts (PHT), San Gorgonio Pass (SGP), and the North Frontal Thrusts (NFT) are in red. (b) Simplified kinematic sketch illustrating how the obliquity of the SAF creates a local shortening (red vector) between the Mojave Block (MB) and Los Angeles (LA). (c) Simplified three-dimensional model across the profile PP′ illustrating how the geometry of the ramp-décollement system partitions the uniform velocity field and controls the amount of shortening and uplift along the various blocks.

[*Rubin et al.*, 1998]. Reconciling all these structures in a self-consistent kinematic model may improve our assessment of seismic hazard in Southern California [e.g., *Gaudemer et al.*, 1995; *Deng and Sykes*, 1997; *Loveless and Meade*, 2011].

The purpose of this study is to better constrain the loading rate on the buried faults below Los Angeles (LA) using geodetic data and a conservative slip-partitioning model. We consider a profile that crosses the Big Bend, the segment of the SAF that is ~N63°W compared to ~N45°W direction along the Coachella

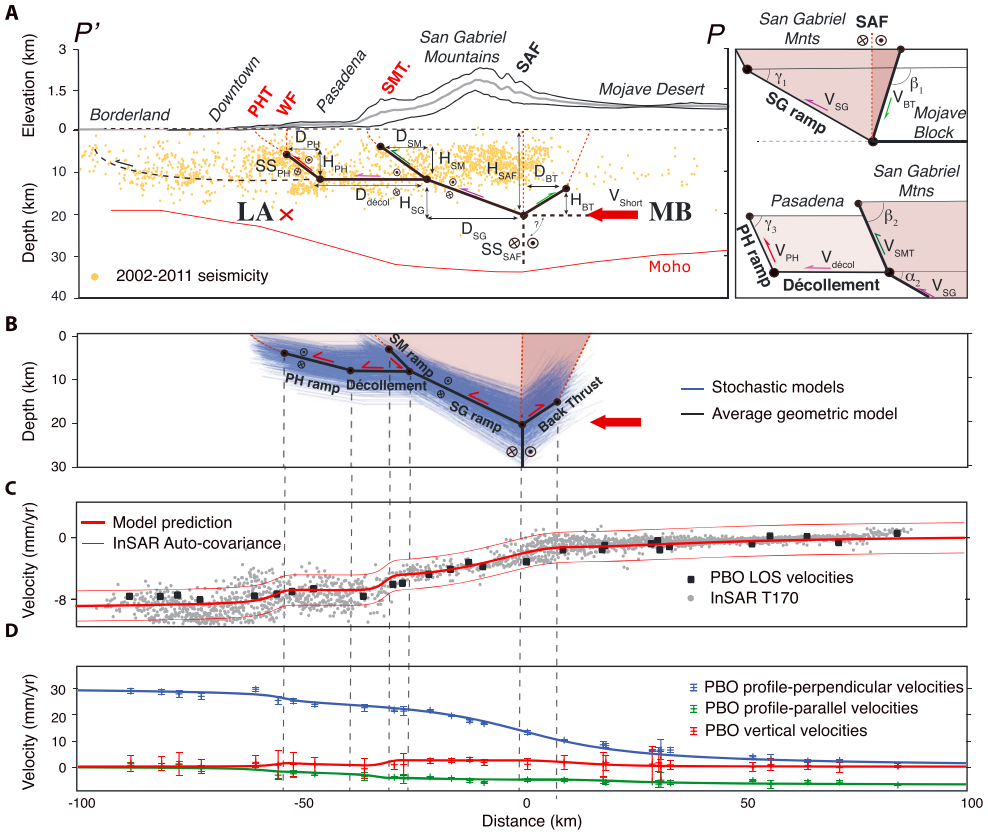

Figure 2. Comparison between the prior and posterior models. (a) Two-dimensional prior model based on the tectonic review along the profile PP′ defined in Figure 1. Black lines (red dashed lines, respectively) represent slipping (locked, respectively) sections of the faults; arrows indicate relative direction of the movement on faults. The SAF is associated with two thick black dashed lines and a question mark as we have no constraints of its deep geometry. We use this configuration and the conservation of motion along each junction to explore the various parameters defined in this figure. Insert is a simplified two-dimensional block model illustrating the relation between the block geometries and longitudinal velocities along the structures. (b) Posterior geometries in agreement with the data (blue lines) and average geometry (black lines). (c) InSAR LOS velocities (grey points) and GPS projected in the LOS direction (black squares) and average model obtained. (d) Profile-perpendicular (blue markers), profile-parallel (green markers), and vertical (red markers) GPS velocities with their associated uncertainties. Average model obtained (blue, green, and red lines) along profiles.

segment (Figure 1). We first identify the broad features of a ramp-décollement system across the San Gabriel mountains (SGM) to explain the topography, seismicity, and tomography data in cross section. We then provide quantitative estimates of the loading rate and the range of geometries consistent with surface velocities observed by interferometric synthetic aperture radar (InSAR) and GPS using a Bayesian framework and assuming conservation of motion across the fault network.

2. Tectonic Constraints

The Big Bend is bounded to the south in the LA Basin by several blind thrust faults and to the north in the Mojave desert by the beginning of the San Bernardino Mountains (SBM). Several observations are in agreement with a large-scale décollement south of the transpressional bend, formed as the result of the obliquity between the relative plate motion and the local orientation of the strike-slip faults (Figure 1b) [*Mount and Suppe*, 1992; *Teyssier and Tikoff*, 1998]. *Crouch and Suppe* [1993] first suggested a low-angle décollement below high-angle faults in the LA region from geological investigations of the Western Transverse Ranges, which has undergone more than 90° of clockwise rotation during the late Cenozoic [*Crouch and Suppe*, 1993; *Nicholson et al.*, 1994; *Atwater*, 1998; *McQuarrie and Wernicke*, 2005], earlier than the activation of the present strike-slip faults. The variation of topography between flat sediments (i.e., the LA Basin) and high topography (i.e., the SBM and SGM) across small distances imply major changes from subhorizontal structures to dipping ramps

(Figures 1c and 2a). The Moho shows a strong thickening of the crust [*Tape et al.*, 2012] from 20 km beneath the LA Basin to 35 km beneath the SGM (Figure 2a). The Sierra Madre Thrusts (SMT), the Whittier Fault (WF), the Elysian Park Thrust (EPT), and the Puente Hills Thrusts (PHT) (Figure 1) may be regarded as partitioned strike-slip and thrust faults above a low-angle décollement [*Shaw and Suppe*, 1996; *Shaw and Shearer*, 1999] at the bottom of the ~15 km thick seismogenic upper crust (Figure 2a). This décollement may extend farther west, as indicated by the uplift of the larger banks, ridges, and islands on the inner Continental Borderland region, offshore LA [*Namson and Davis*, 1988; *Davis et al.*, 1989]. Numerous earthquakes in this area have pure dip-slip thrust focal mechanisms and their hypocenter locations cluster between 10 and 15 km depth along shallow northeast dipping planes [*Astiz and Shearer*, 2000]. At the junction between the Mojave and the Coachella segment, *Yule and Sieh* [2003] inferred from geological measurements, from the southward deepening of microseismicty (~10°S [*Corbett*, 1984]) and from several small, deep earthquakes with shallow nodal planes [*Webb and Kanamori*, 1985], that the crustal structure of the complex San Gorgonio Pass (SGP) (Figure 1) may also involve a low-angle décollement at depth that undercuts the North Frontal Thrust (NFT) and decouples the upper and the lower crust. More recently, results from the Los Angeles Region Seismic Experiment refraction surveys [*Kohler*, 1999; *Fuis et al.*, 2001a, 2001b, 2012] have confirmed the presence of a low-angle reflective layer below the SGM, which originates at the SAF and terminates near the hypocenters of the 1971 San Fernando and 1987 Whittier Narrows thrust earthquakes [*Fuis et al.*, 2003]. This large-scale décollement may branch on the SAF in a weak upper mantle, with a depth commensurate with the width of the SGM (~25 km), following the old suture zone created by the subduction of the Farallon Plate beneath the NAP [*Fuis et al.*, 2012], and may terminate offshore (Figures 1c and 2a).

3. Deformation Data

To constrain the activity and geometry of the structures below Los Angeles, we use geodetic data within a 60 km wide and 200 km long swath oriented perpendicular to the local azimuth of the SAF. These include the three-dimensional GPS velocity field from the Plate Boundary Observatory (PBO) and a line-of-sight (LOS) velocity map derived from Envisat and ERS descending pass spanning 18 years [*Liu et al.*, 2014]. The InSAR data analysis is based on a small baseline approach and includes a series of corrections for atmospheric, orbital errors, and oscillator frequency drift (cf. supporting information).

4. Description of the Model

We assume that the shallow vertical and high-angle faults, which formed a complex three-dimensional system at the surface, are locked during the interseismic period, while the segments that connect the downdip end of locked faults, at the bottom of the seismic upper crust, slip aseismically, partitioning the observed uniform velocity field (Figure 1).

Several scenarios might be possible to accommodate shortening across the mountain range including a ramp-décollement system [*Crouch and Suppe*, 1993], distributed deformation [*Wilcox et al.*, 1973], and out-of-sequence thrusts within the wedge [e.g., *Whipple et al.*, 2016]. Following our interpretation of geological, seismological, and surface deformation data, we divide the region in three rigid blocks delimited by two triple junctions and one frontal ramp (Figures 1c and 2a). The first ramp and the back thrust extrude the San Gabriel and the San Bernardino ranges (Figure S2b), while a flat décollement lies under the LA Basin (Figure S2c), connecting to the downdip end of the SM and the PH ramps (Figure S2d). As we have no constraints on the geometry and the mechanics of the deep-seated shear zone below the SAF, we model the motion by a horizontal semi-infinite dislocation, limited to the west by the SAF (Figure 2a). The surface strain due to the strike-slip component, SS_{SAF}, is not influenced by the dip angle of the fault (Figure S3) [*Segall*, 2010]. However, the longitudinal component on this flat structure, V_{short}, can accommodate the local convergence caused by the oblique angle between the SAF and far-field plate motion near the Big Bend (Figures 1b and 2a). We also allow a strike-slip component on the ramp-décollement system by adding a strike-slip motion on a semi-infinite dislocation, SS_{PH}. The deep-seated strike-slip motion below the SAF locking depth that controls the far-field motion is equal to the sum of strike-slip rates on the two dislocations, $SS_{SAF} + SS_{PH}$. We estimate the depth of locking H_{SAF} of the SAF. For other segments, we estimate the horizontal and the vertical distance between the triple junction and the tip of the segments (D and H) (Figure 2a).

5. Slip-Partitioning Constraints

Geodetic data offer limited constraints on fault geometry at depth [*Savage*, 1990; *Segall*, 2010]. But slip partitioning brings additional kinematic constraints to enforce long-term compatibility of displacements along various segments of faults. At a triple junction, the partitioning of the velocity V_1 along a deep-seated fault into a velocity V_2 along a ramp and V_3 along a back fault implies the conservation of the horizontal and vertical motion along the three segments (Figures 2a and S1). In analogy to the fault-bend fold models of *Suppe* [1983], we consider a kinematic model that conserves motion across the block boundaries. Assuming rigid blocks and no tilt of the hanging wall, the ratio of slip velocities on the faults bounding the blocks is

$$\begin{aligned} \frac{V_2}{V_1} &= \frac{\sin(\beta - \gamma + \alpha)}{\sin(\beta - \gamma)} \\ \frac{V_3}{V_1} &= \frac{\sin \alpha}{\sin(\beta - \gamma)}, \end{aligned} \tag{1}$$

where γ and β are the dip angles of the ramp and the back fault, respectively. We denote α the angle between the deep-seated fault and the ramp.

6. Prior Assumptions

Dip angles are determined from the horizontal and vertical distances, D and H, and the along-dip components of slip are thus constrained using the conservation of motion across each junctions from equation 1 (cf. supporting information).

We first define the convergence across the fault system, V_{short}, as the local horizontal shortening perpendicular to the Mojave segment of the SAF (Figures 1b, 2, and S2a) measured by the GPS between the Mojave Block and LA encompassing the profile PP′. Our prior assumption is that the deep-seated rates of motion are normally distributed centered on the far-field horizontal motion (Figure 1b). This gives a shortening rate of $V_{\text{short}} = 7$ mm/yr with a 1σ uncertainty of 1.5 mm/yr and a deep-seated strike-slip motion of 26 mm/yr with an uncertainty of 5 mm/yr. For other parameters, we assume uniform prior distributions bounded by realistic values. According to the geological and seismological setting, we force the décollement below the LA Basin to be horizontal (Figure 2a). Prior distributions for all parameters are summarized in Table S2.

7. Inversion Method

We explore the range of models allowed by geodetic data and derive the posterior probability describing the full ensemble of possible models, $p(\mathbf{m}|\mathbf{d})$, that explain the observations, $\mathbf{d}$, and agree with a prior knowledge, $p(\mathbf{m})$, implementing a Bayesian approach [*Minson et al.*, 2013; *Jolivet et al.*, 2015; *Lin et al.*, 2015; *Daout et al.*, 2016], such as

$$p(\mathbf{m}|\mathbf{d}) \propto p(\mathbf{m}) \exp\left[-\frac{1}{2}(\mathbf{d} - \mathbf{g}(\mathbf{m}))^T \mathbf{C}_D^{-1}(\mathbf{d} - \mathbf{g}(\mathbf{m}))\right], \tag{2}$$

where $\mathbf{d}$ is the data vector, $\mathbf{m}$ is the vector of model parameters, $\mathbf{C}_D$ is the covariance matrix of the data, and $\mathbf{g}(\mathbf{m})$ is the surface displacements predicted from model $\mathbf{m}$. The model parameters include the ones previously described for geometry and slip rates and the InSAR and GPS reference frames. We add an unknown azimuth linear trend to InSAR data that ties far-field LOS velocities to GPS data (Table S2). As the InSAR velocity field profile flattens in the far field, we did not add a quadratic term [*Chaussard et al.*, 2015]. The data vector, $\mathbf{d}$, is made of the LOS displacement rates, the GPS vertical velocities, and the GPS horizontal velocities projected into profile-perpendicular and profile-parallel components (Table S1). The data covariance matrix includes the variance of the GPS and InSAR measurements on its diagonal and InSAR data spatial correlation in the off-diagonal components (cf. supporting information and Figures S4 and S5).

We then draw random samples from prior distributions previously defined (Table S2) and evaluate the posterior probability density functions (PDFs) using the Metropolis algorithm, implemented in the *PYmC* library [*Patil et al.*, 2010], guided by the geodetic data and the associated uncertainties.

8. Posterior Models

We sample the model space with 40,000 samples, rejecting the first 30,000 to minimize the effect of the initial model. A large range of possible models in agreement with the data and the conservation of motion are shown in blue lines in Figure 2b. The comparison between the prior and posterior models is summarized in Table S2 and Figure S6. Except for parameters $D_{décol}$, D_{SM}, and H_{PH}, all posterior PDFs show normal distributions centered on the mean models (red vertical lines in Figure S6) away from the prior limits. Posterior PDFs are narrowed in comparison to the prior PDFs highlighting the gain of information from the data and the conservation of motion. The sensitivity of InSAR to vertical deformation and its dense spatial sampling makes it a valuable complementary data sets to GPS. We compare these results with inversions that consider GPS alone in the supporting information (Figures S6 and S7). The comparison between surface observations and predictions from the mean value of the posterior model is shown in Figures 2c and 2d. There is in general a good agreement between observations and predictions. Predicted velocity maps and GPS vectors are also presented in Figure S8, while the full posterior covariance of the model parameters and the joint posterior probabilities between slip rates and locking depths are displayed in Figures S9 and S10. The GPS residuals are smaller than 1 mm/yr, indicating that the model explains horizontal deformation well. In contrast, InSAR residuals reveal subsidence within the LA Basin bounded by the Whittier and the Palos Verdes Faults (Figures 2b and S8).

The average posterior model indicates a locking depth of 20 ± 3.5 km and 3.5 ± 2.5 km for the SAF and Whittier-Puente Hills fault system, respectively (all the uncertainties are documented $\pm 1\sigma$). These depths are associated with strike-slip rates of 25.5 ± 0.5 mm/yr on the SAF and 3.1 ± 0.6 mm/yr on the WF. We find that the 6.6 ± 0.6 mm/yr of shortening rate is partitioned between 3.1 ± 0.5 mm/yr on the 40 ± 5°SW dipping back thrust segment and 4.7 ± 0.7 mm/yr on the 25 ± 5°NE ramp segment below the SGM. Then, slip on the ramp partitions into 2.7 ± 0.9 mm/yr on the 48 ± 5°NE Sierra Madre ramp and 2.5 ± 1.0 mm/yr on the 16 ± 10°NE dipping Puente Hills ramp (Figure 2b). The 8 ± 3.5 km depth flat décollement below the LA Basin connecting the downdip end of the PH ramp with the tip of the SG ramp creeps at 2.4 ± 0.7 mm/yr. To summarize, among the 6.6 ± 0.6 mm/yr of local shortening across the profile, the back thrust structure accommodates around 2.4 mm/yr of horizontal convergence, while the SMT and the PHT absorb 1.8 mm/yr and 2.4 mm/yr of shortening, respectively.

We explore the influence of adding a strike-slip creeping segment on the SAF between the junction of SG ramp with the SAF and a shallow locking depth of the SAF, but our results indicate a strike-slip motion on this shallower segment close to zero.

9. Discussion

The average slip rates and the most likely geometry of the fault system is shown in Figures 3 and 2b. Note that although our model is two-dimensional, it explains the three-dimensional interseismic velocity field remarkably well (Figure S8).

Our mean posterior model indicates a deep-seated strike-slip rate of 28.6 ± 0.5 mm/yr partitioned into 25.5 ± 0.5 mm/yr on the SAF, locked at 20 ± 3.5 km depth, and 3.1 ± 0.6 mm/yr on the ramp-décollement system, creeping from the SG-SAF junction to the tip of the PH ramp at 3.5 ± 2.5 km depth. The rate of the SAF is near the high end of the range of rates previously estimated for the Mojave section of the SAF using single fault models [e.g., *Savage and Lisowski*, 1995], two-dimensional, GPS-constrained, block models [e.g., *Shen et al.*, 1996; *McCaffrey*, 2005; *Meade and Hager*, 2005], or viscoelastic half-space models [e.g., *Tong et al.*, 2014]. Long-term geologic slip rates along the SAF range from 24.5 ± 3.5 mm/y [*Weldon and Sieh*, 1985] in the Cajon Pass to 35 ± 7 mm/y in the Pallett Creek [*Salyards et al.*, 1992]. The modeled strike-slip component on the ramp-décollement system is also comparable with the 2.5 ± 0.5 mm/yr of long-term strike-slip motion measured on the Whittier fault zone [*Walls et al.*, 1998]. The deep-seated strike-slip motion is in agreement with geometry of the Big Bend. If we consider 34 mm/yr of strike-slip component along the central segment observed both geologically and geodetically [*Sieh and Jahns*, 1984; *Barbot et al.*, 2013], the 25° of change of azimuth of the SAF from the Central segment to the Big Bend would create a strike-slip rate along the Mojave of ~30 mm/yr.

The average posterior locking depth of the SAF is slightly deeper than the seismogenic depth of 15 km estimated from the maximum depth of earthquakes [*Hauksson et al.*, 2012] but comparable to the locking depth of 20 km adopted by *McCaffrey* [2005] based on a regional misfit between a block model and GPS data.

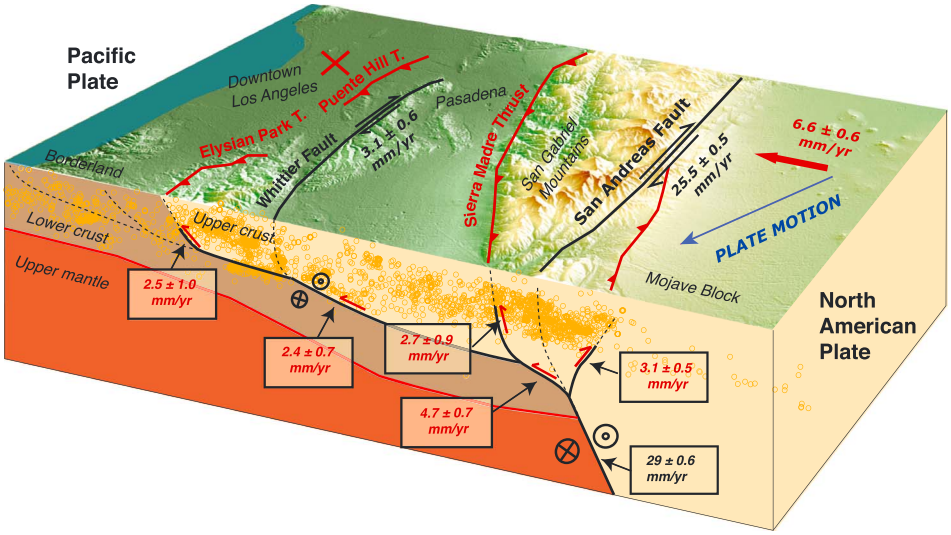

Figure 3. Three-dimensional schematic block model across the SGM [after *Fuis et al.*, 2001b] superimposed to the digital elevation model, the seismicity (yellow dots), the Moho model (red line), and interpreted active faults summarizing the average interseismic strike-slip (back arrows) and dip-slip (red arrows) rates extracted from the Bayesian exploration. Shallow faults (dashed lines) that formed a complex three-dimensional system at the surface [*Plesch et al.*, 2007] are locked during the interseismic period, while the ramp-décollement system (solid lines) decouples the upper crust from the lower crust and partitioned the observed uniform velocity field (blue vector) at the downdip end of the structures.

The difference of rheology between the Los Angeles sedimentary basin and the Mojave block may explain the contrast of locking depths between the SAF and the PH ramp. Locking depth below the LA sedimentary basin may be underestimated as we do not take into account these rheological effects [*Argus et al.*, 2005], while viscoelastic effects may decrease the San Andreas strike-slip rate in comparison to simple elastic models [*Tong et al.*, 2014]. However, dip-slip rates obtained by our exploration are in good agreement with the paleoseismological and geological slip rates without the need of introducing viscoelastic effects. Below LA, paleoseismology indicates [0.4–1.7] mm/yr and [0.6–1.6] mm/yr of quaternary slip rates on the PHT [*Shaw et al.*, 2002; *Dolan et al.*, 2003] and the EPT [*Shaw and Suppe*, 1996; *Oskin et al.*, 2000], respectively, while long-term slip rates of the central SMT are within the range of [2.0–5.5] mm/yr [*Dolan et al.*, 1995; *Walls et al.*, 1998]. In comparison, we constrain 2.5 $\pm$ 1.0 mm/yr on the frontal ramp at the roots of PHT and the EPT, creeping until 3.5 $\pm$ 2.5 km depth, and 2.7 $\pm$ 0.9 mm/yr of creep below the Sierra Madre thrusts up to 3 $\pm$ 2.5 km depth, at the front of the San Gabriel ranges. Note that these inverted dip-slip rates at depth, perpendicular to the profile, might be released at the surface by pure thrust motion or by strike slip on oblique faults, as, for instance, the Raymond and San Jose faults extending west-southwest and forming a complex three-dimensional system [*Walls et al.*, 1998].

Posterior PDFs show that the strike-slip rate of the SAF does not trade-off with its locking depth but correlates with the strike-slip rate of the PH ramp (Figures S9 and S10). GPS data provide a reference on the horizontal component of ground displacement. Far-field strike-slip rate, $SS_{SAF}+SS_{PH}$, and shortening rate, V_{short}, are identically constrained with and without InSAR data (Figures S6 and S7). This shows that the GPS velocity field is dense enough to constrain the deformation gradient and thus the locking depth of the SAF. We also observe a correlation of the locking depth of the SAF with the parameters H_{SG} and D_{SG}, and thus the dip angle of the SG ramp (Figure S9). Overall, the posterior correlation matrix indicates strong correlations between parameters D and H of the various dislocations as they control the geometry of the ramps and the amount of dip-slip motion. Small variations of dip angles results in significant changes in vertical velocities. Without InSAR data, parameters H and D of the SG, SM, and PH ramps are not well constrained as they indicate posterior PDFs close to the prior uniform distributions (Figure S6). Average posterior model indicates a deeper depth for the tip of SG ramp and a vertical gradient that concentrates at the front of the Puente Hills ranges (Figure S7). Due to a high sensitivity to vertical movements, InSAR data force the partitioning of the shortening rates between the SM and the PH ramps, which is in agreement with the differential topography and vertical velocity between the SGM and the LA Basin (Figure 1a), as well as the long-term respective slip rates of the SMT and the PHT [*Dolan et al.*, 1995]. In comparison to previous studies, by inverting both GPS and InSAR data

simultaneously, we improve the sampling of the surface displacement field, especially in the vertical direction, better constraining the geometry of the ramp-décollement system and the intervening slip rates at depth.

The 3.1 ± 0.5 mm/yr of slip along the back thrust structure is not associated with any identified surface trace north of the SGM but may correspond to the extension of the North Frontal Thrusts below the San Bernardino mountains (Figure 1). However, it is difficult to conclude about the nature of this structure, which might represent distributed deformation formed in a fault-bend fold [*Suppe*, 1983], or a back thrust part of a flower structure (Figure 3). The structure accommodates the slip incompatibility between the shortening rate (V_{short}) and the ramp (V_{SG}) to conserve motion across the fault network. It is required to fit fault-perpendicular and vertical GPS velocities and the displacement gradient in InSAR data north of the SAF.

At greater depth, the local convergence across the profile may be accommodated by shear zone extending northward of the SAF [e.g., *Bowman et al.*, 2003], following the old suture zone formed by the subduction of the Farallon Plate beneath the NAP that connects the Carrizo plain in the north to the Golf of California in the south [*Teyssier and Tikoff*, 1998; *Fuis et al.*, 2012; *Wang et al.*, 2013; *Pikser et al.*, 2012]. In this scenario, slip on this mantle structure might not create detectable surface displacements due to the large differences in viscosity between the upper mantle and the lower crust, the isostatic effects of this long-wavelength slab or the low angle of this deep-seated structure. In an alternative scenario, the upper mantle boundary between the North America and the Pacific plate may follow the San Andreas Fault from the central segment, in the north, to the SJF, in the south. In this case, the transpressional bend may only reside in the crust and may not be associated with motion in the mantle. Our proposed model is compatible with both scenarios, which cannot be differentiated from geodetic studies alone.

10. Conclusion

We develop a novel way to explore the compatibility of geodetic velocities with a long-term kinematic model that conserves motion along and across a fault system. We apply the method to understand slip partitioning around the Big Bend of the SAF and the loading of buried faults below the LA metropolitan area. We start from a simplified prior geometry of connected faults beneath the SGM section of the PAP-NAP plate boundary. Using the conservation of motion across fault junctions as a prior constraint, we then propagate the far-field GPS field on the ramp-décollement system and explore the parameter space of fault geometries and slip rates that satisfy the InSAR and GPS velocity fields. Our most likely model suggests the existence of a flat décollement below Metropolitan Los Angeles bounded by two steeper ramps under the Sierra Madre and the Puente Hills that are creeping below a shallow locking depth. The proposed fault network geometry and kinematics also includes slip along a SW dipping back thrust connecting to the SAF and accommodating part of convergence between the Mojave block and the San Gabriel ranges. This study underlines the importance of understanding first-order fault geometry for geodetic models [*Daout et al.*, 2016; *Qiu et al.*, 2016] and represents another step forward toward bridging the gap between earthquake cycle modeling and structural geology.

Acknowledgments

S.D. is supported by the Grenoble Innovation Recherche (AGIR) fellowship, the CNRS Mastodons computing facilities, and the Labex OSUG@2020 University of Grenoble project. S.B. is funded by the National Research Foundation Singapore under its Singapore NRF Fellowship scheme (National Research Fellow award NRF-NRFF2013-04), by the Earth Observatory of Singapore, and the National Research Foundation Singapore and the Singapore Ministry of Education under the Research Centres of Excellence initiative. G.P. and Z.L. are supported under the contract with the National Aeronautics and Space Administration at the Jet Propulsion Laboratory, California Institute of Technology. GPS data are from the Plate Boundary Observatory (PBO) operated by UNAVCO for EarthScope (http://www.earthscope.org). The SAR data set was provided by the European Space Agency (ESA) in the framework of WINSAR. InSAR velocity map is available from the authors upon request. We are grateful to Paul Tapponnier and Kerry Sieh for stimulating discussions about the tectonic and geological setting. We thank Editor Andrew Newman, Estelle Chaussard, Brendan Meade, and an anonymous reviewer for their constructive criticism that has significantly improved the manuscript. This is SCEC Contribution #7112.

References

Argus, D. F., M. B. Heflin, G. Peltzer, F. Campe, and F. H. Webb (2005), Interseismic strain accumulation and anthropogenic motion in metropolitan Los Angeles, *J. Geophys. Res.*, *110*, B04401, doi:10.1029/2003JB002934.

Astiz, L., and P. M. Shearer (2000), Earthquake locations in the inner continental borderland, offshore southern California, *Bull. Seismol. Soc. Am.*, *90*, 425–449.

Atwater, T. M. (1998), Plate tectonic history of Southern California with emphasis on the Western Transverse Ranges and Santa Rosa Island, in *Contributions to the Geology of the Northern Channel Islands*, edited by P. W. Weigand, pp. 1–8, Am. Assoc. Pet. Geol., Southern California.

Barbot, S., P. Agram, and M. D. Michele (2013), Change of apparent segmentation of the San Andreas Fault around Parkfield from space geodetic observations across multiple periods, *J. Geophys. Res. Solid Earth*, *118*, 6311–6327, doi:10.1002/2013JB010442.

Bock, Y., et al. (1997), Southern California permanent GPS geodetic array: Continuous measurements of regional crustal deformation between the 1992 Landers and 1994 Northridge earthquakes, *J. Geophys. Res.*, *102*(B8), 18,013–18,033.

Bowman, D., G. King, and P. Tapponnier (2003), Slip partitioning by elastoplastic propagation of oblique slip at depth, *Science*, *300*(5622), 1121–1123.

Chaussard, E., R. Bürgmann, H. Fattahi, R. Nadeau, T. Taira, C. Johnson, and I. Johanson (2015), Potential for larger earthquakes in the east San Francisco Bay area due to the direct connection between the Hayward and Calaveras Faults, *Geophys. Res. Lett.*, *42*, 2734–2741, doi:10.1002/2015GL063575.

Corbett, E. (1984), Seismicity and crustal structure of Southern California: Tectonic implications for the transfer of Baja California to the Pacific Plate and estimates of the Pacific-North America motion, PhD thesis, Calif. Inst. of Technol., Pasadena, Calif.

Crouch, J. K., and J. Suppe (1993), Late Cenozoic tectonic evolution of the Los Angeles Basin and inner California borderland: A model for core complex-like crustal extension, *Geol. Soc. Am. Bull.*, *105*, 1415–1434.

Daout, S., R. Jolivet, C. Lasserre, M.-P. Doin, S. Barbot, P. Tapponnier, G. Peltzer, A. Socquet, and J. Sun (2016), Along-strike variations of the partitioning of convergence across the Haiyuan Fault system detected by InSAR, *Geophys J. Int.*, *205*(1), 536–547.

Davis, T. L., J. Namson, and R. F. Yerkes (1989), A cross section of the Los Angeles area: Seismically active fold and thrust belt, the 1987 Whittier narrows earthquake, and earthquake hazard, *J. Geophys. Res.*, *94*(B7), 9644–9664.

Deng, J., and L. R. Sykes (1997), Evolution of the stress field in southern California and triggering of moderate-size earthquakes: A 200-year perspective, *J. Geophys. Res.*, *102*(B5), 9859–9886.

Dolan, J. F., K. Sieh, T. K. Rockwell, R. S. Yeats, J. Shaw, J. Suppe, G. J. Huftile, and E. M. Gath (1995), Prospects for larger or more frequent earthquakes in the Los Angeles Metropolitan Region, *Science*, *267*, 199–205.

Dolan, J. F., S. A. Christofferson, and J. H. Shaw (2003), Recognition of paleoearthquakes on the Puente Hills blind thrust fault, California, *Science*, *300*(5616), 115–118.

Fuis, G., T. Ryberg, W. Lutter, and P. Ehlig (2001a), Seismic mapping of shallow fault zones in the San Gabriel mountains from the Los Angeles region seismic experiment, Southern California, *J. Geophys. Res.*, *106*(B4), 6549–6568.

Fuis, G., T. Ryberg, N. Godfrey, D. Okaya, and J. Murphy (2001b), Crustal structure and tectonics from the Los Angeles Basin to the Mojave Desert, Southern California, *Geology*, *29*, 15–18.

Fuis, G., D. S. Scheirer, V. E. Langenheim, and M. D. Kohler (2012), A new perspective of the geometry of the San Andreas Fault in Southern California and its relationship to the lithospheric structure, *Bull. Seismol. Soc. Am.*, *102*, 236–251.

Fuis, G. S., et al. (2003), Fault systems of the 1971 San Fernando and 1994 Northridge earthquakes, southern California: Relocated aftershocks and seismic images from LARSE II, *Geology*, *31*(2), 171–174.

Furlong, K., and W. D. Hugo (1989), Geometry and evolution of the San Andreas Fault zone in Northern California, *J. Geophys. Res.*, *94*(B3), 3100–3110.

Gaudemer, Y., P. Tapponier, B. Meyer, G. Peltzer, G. Shunmin, C. Zhitai, D. Huagung, and I. Cifuentes (1995), Partionning of crustal slip between linked, active faults in the eastern Qilian Shan, and evidence for a major seimic gap, the "Tianzhu Gap", on the western Haiyuan Fault, Gansu (China), *Geophys. J. Int.*, *120*, 599–645.

Hauksson, E., W. Yang, and P. Shearer (2012), Waveform relocated earthquake catalog for southern California (1981 to 2011), *Bull. Seismol. Soc. Am.*, *102*, 2239–2244.

Jolivet, R., M. Simons, P. Agram, Z. Duputel, and Z.-K. Shen (2015), Aseismic slip and seismogenic coupling along the Central San Andreas Fault, *Geophys. Res. Lett.*, *42*, 297–306, doi:10.1002/2014GL062222.

Kohler, M. D. (1999), Lithospheric deformation beneath the San Gabriel Mountains in the Southern California transverse ranges, *J. Geophys. Res.*, *104*(B7), 15,025–15,041.

Lin, Y., R. Jolivet, M. Simons, P. Agram, H. Martens, Z. Li, and S. Lodi (2015), High interseismic coupling in the Eastern Makran (Pakistan) subduction zone, *Earth Planet. Sci. Lett.*, *420*, 116–126.

Lisowski, M., J. C. Savage, and W. Prescott (1991), The velocity field along the San Andreas Fault in central and southern California, *J. Geophys. Res.*, *96*(B5), 8369–8389.

Liu, Z., P. Lundgren, and Z. Shen (2014), Improved imaging of southern California crustal deformation using InSAR and GPS, SCEC Contribution 2038 presented at SCEC Annual Meeting, Palm Springs, California.

Loveless, J. P., and B. J. Meade (2011), Stress modulation on the San Andreas Fault by interseismic fault system interactions, *Geology*, *39*(11), 1035–1038.

McCaffrey, R. (2005), Block kinematics of the Pacific-North America plate boundary in the southwestern United States from inversion of GPS, seismological, and geologic data, *J. Geophys. Res.*, *110*, B07401, doi:10.1029/2004JB003307.

McQuarrie, N., and B. P. Wernicke (2005), An animated tectonic reconstruction of southwestern North America since 36 Ma, *Geosphere*, *1*(3), 147–172.

Meade, B. J., and B. H. Hager (2005), Block models of crustal motion in southern California constrained by GPS measurements, *J. Geophys. Res.*, *110*, B03403, doi:10.1029/2004JB003209.

Minson, S., M. Simons, and J. Beck (2013), Bayesian inversion for finite fault earthquake source models; I—Theory and algorithm, *Geophys. J Int.*, *194*, 1701–1726, doi:10.1093/gji/ggt180.

Mount, V. S., and J. Suppe (1987), State of stress near the San Andreas Fault: Implications for wrench tectonics, *Geology*, *15*(12), 1143–1146.

Mount, V. S., and J. Suppe (1992), Present-day stress orientations adjacent to active strike-slip faults: California and Sumatra, *J. Geophys. Res.*, *97*, 11,995–12,013.

Namson, J. S., and T. L. Davis (1988), Seismically active fold and thrust belt in the San Joaquin Valley, central California, *Geol. Soc. Am. Bull.*, *100*, 257–273.

Nicholson, C., C. C. Sorlien, T. Atwater, J. C. Crowell, and B. P. Luyendyk (1994), Microplate capture, rotation of the western transverse ranges, and initiation of the San Andreas transform as a low-angle fault system, *Geology*, *22*(6), 491–495.

Oskin, M., K. Sieh, T. Rockwell, G. Miller, P. Guptill, M. Curtis, S. McArdle, and P. Elliot (2000), Active parasitic folds on the elysian park anticline: Implications for seismic hazard in central Los Angeles, California, *Geol. Soc. Am. Bull.*, *112*(5), 693–707.

Patil, A., D. Huard, and C. J. Fonnesbeck (2010), PyMC: Bayesian stochastic modelling in python, *J. Stat. Software*, *35*(4), 1–81.

Pikser, J. E., D. W. Forsyth, and G. Hirth (2012), Along-strike translation of a fossil slab, *Earth Planet. Sci. Lett.*, *331*, 315–321.

Plesch, A., et al. (2007), Community Fault Model (CFM) for Southern California, *Bull. Seismol. Soc. Am.*, *97*(6), 1793–1802.

Qiu, Q., E. M. Hill, S. Barbot, J. Hubbard, W. Feng, E. O. Lindsey, L. Feng, K. Dai, S. V. Samsonov, and P. Tapponnier (2016), The mechanism of partial rupture of a locked megathrust: The role of fault morphology, *Geology*, *44*(10), 875–878.

Rubin, C. M., S. C. Lindvall, and T. K. Rockwell (1998), Evidence for large earthquakes in metropolitan Los Angeles, *Science*, *281*, 398–402.

Salyards, S. L., K. E. Sieh, and J. L. Kirschvink (1992), Paleomagnetic measurement of nonbrittle coseismic deformation across the San Andreas Fault at Pallett Creek, *J. Geophys. Res.*, *97*(B9), 12,457–12,470.

Savage, J., and M. Lisowski (1995), Interseismic deformation along the San Andreas Fault in southern California, *J. Geophys. Res.*, *100*(B7), 12,703–12,717.

Savage, J. C. (1990), Equivalent strike-slip earthquakes cycles in half-space and lithosphere-asthenosphere Earth models, *J. Geophys. Res.*, *95*(B4), 4873–4879.

Segall, P. (2010), *Earthquake and Volcano Deformation*, Princeton Univ. Press, Princeton, N. J.

Shaw, J., and J. Suppe (1996), Earthquakes hazards of active blind-thrust faults under the central Los Angeles basin, California, *J. Geophys. Res.*, *101*, 8623–8642.

Shaw, J. H., and P. M. Shearer (1999), An elusive blind-thrust fault beneath metropolitan Los Angeles, *Science*, *283*(5407), 1516–1518.

Shaw, J. H., A. Plesch, J. F. Dolan, T. L. Pratt, and P. Fiore (2002), Puente hills blind-thrust system, Los Angeles, California, *Bull. Seismol. Soc. Am.*, *92*(8), 2946–2960.

Shen, Z.-K., D. D. Jackson, and B. X. Ge (1996), Crustal deformation across and beyond the Los Angeles Basin from geodetic measurements, *J. Geophys. Res.*, *101*, 27,957–27,980.
Sieh, K. (1978), Slip along the San Andreas Fault associated with the great 1857 earthquake, *Bull. Seismol. Soc. Am.*, *68*, 1421–1428.
Sieh, K. E., and R. H. Jahns (1984), Holocene activity of the San Andreas Fault at Wallace Creek, California, *Geol. Soc. Am. Bull.*, *95*(8), 883–896.
Suppe, J. (1983), Geometry and kinematics of fault-bend folding, *Am. J. Sci.*, *283*, 684–721.
Tape, C., A. Plesch, J. H. Shaw, and H. Gilbert (2012), Estimating a continuous Moho surface for the California unified velocity model, *Seismol. Res. Lett.*, *83*, 728–735.
Teyssier, C., and B. Tikoff (1998), Strike-slip partitioned transpression of the San Andreas Fault system: A lithospheric-scale approach, in *Continental Transpressional and Transtensional Tectonics*, edited by R. E. Holdsworth, R. A. Strachan, and J. F. Dewey, pp. 143–158, Geol. Soc., London, U. K.
Tong, X., D. T. Sandwell, and B. Smith-Konter (2013), High-resolution interseismic velocity data along the San Andreas Fault from GPS and InSAR, *J. Geophys. Res. Solid Earth*, *118*, 369–389, doi:10.1029/2012JB009442.
Tong, X., B. Smith-Konter, and D. T. Sandwell (2014), Is there a discrepancy between geological and geodetic slip rates along the San Andreas Fault system?, *J. Geophys. Res. Solid Earth*, *119*, 2518–2538, doi:10.1002/2013JB010765.
Toppozada, T. R., D. M. Branum, M. S. Reichle, and C. L. Hallstrom (2002), San Andreas Fault zone, California: M $\geq$ 5.5 earthquake history, *Bull. Seismol. Soc. Am.*, *92*(7), 2555–2601.
Walls, C., T. Rockwell, K. Mueller, Y. Bock, S. Williams, J. Pfanner, J. Dolan, and P. Fang (1998), Escape tectonics in the Los Angeles metropolitan region and implications for seismic risk, *Nature*, *394*, 356–360.
Wang, Y., D. W. Forsyth, C. J. Rau, N. Carriero, B. Schmandt, J. B. Gaherty, and B. Savage (2013), Fossil slabs attached to unsubducted fragments of the Farallon plate, *Proc. Natl. Acad. Sci. U.S.A.*, *110*(14), 5342–5346.
Webb, T., and H. Kanamori (1985), Earthquake focal mechanisms in the eastern Transverse Ranges and San Emigdio Mountains, southern California, and evidence for a regional decollement, *Bull. Seismol. Soc. Am.*, *75*, 735–757.
Weldon, R. J., and K. E. Sieh (1985), Holocene rate of slip and tentative recurrence interval for large earthquakes on the San Andreas Fault, Cajon Pass, Southern California, *Geol. Soc. Am. Bull.*, *96*(6), 793–812.
Whipple, K. X., M. Shirzaei, K. V. Hodges, and J. R. Arrowsmith (2016), Active shortening within the Himalayan orogenic wedge implied by the 2015 Gorkha earthquake, *Nat. Geosci.*, *9*, 711–716.
Wilcox, R. E., T. T. Harding, and D. Seely (1973), Basic wrench tectonics, *AAPG Bull.*, *57*(1), 74–96.
Yule, D., and K. Sieh (2003), Complexities of the San Andreas fault near San Gorgonio Pass: Implications for large earthquakes, *J. Geophys. Res.*, *108*(B11), 2548, doi:10.1029/2001JB000451.